



Cylindrical cavity expansion approximations using different constitutive models for the target material

International Journal of Protective Structures

1–27

© The Author(s) 2017

Reprints and permissions:

sagepub.co.uk/journalsPermissions.nav

DOI: 10.1177/2041419617741321

journals.sagepub.com/home/prs



Joakim Johnsen¹ , Jens Kristian Holmen¹,
Thomas L Warren² and Tore Børvik¹

Abstract

In this article, we investigate the results obtained using different constitutive models for the solution of the cylindrical cavity expansion problem under plane strain conditions. The cylindrical cavity expansion solutions are employed with the cylindrical cavity expansion approximation to obtain ballistic limit and residual velocities for ductile metals perforated by rigid projectiles. Many of the previously developed cylindrical cavity expansion approximations use simplified constitutive models. However, in the present work, we first extend the cylindrical cavity expansion theory with the Voce strain hardening rule, before we utilize three different strain hardening constitutive models in cylindrical cavity expansion calculations to predict ballistic limit and residual velocities of aluminum and steel target plates struck by rigid projectiles. The results show that when strain hardening is accurately represented by the constitutive models until necking in a uniaxial tension test, all cylindrical cavity expansion models predict ballistic limit velocities that are close to the experimental data.

Keywords

Ductile hole growth, perforation, cylindrical cavity expansion theory, ballistic impact, impact

Introduction

Over the years, both the spherical cavity expansion (SCE) approximation for deep penetration and the cylindrical cavity expansion (CCE) approximation for ductile hole growth perforation have provided reasonable results in predicting the associated experimental data. Both quasi-static SCE and CCE approximations were originally developed by Bishop et al. (1945) to model rigid conical-nosed punches quasi-statically indenting various metallic blocks. In their work, they found that radial stresses in the range of 3 to 4 times the yield strength of the indented materials were required

¹Structural Impact Laboratory (SIMLab), Department of Structural Engineering, Norwegian University of Science and Technology (NTNU), Trondheim, Norway

²Thomas L. Warren, Ph.D., Inc., Albuquerque, NM, USA

Corresponding author:

Joakim Johnsen, Structural Impact Laboratory (SIMLab), Department of Structural Engineering, Norwegian University of Science and Technology (NTNU), 7491 Trondheim, Norway.

Email: joakim.johnsen@ntnu.no

to expand a cavity (Rosenberg and Dekel, 2012). These analytical results were also found to be in good agreement with experimental data. The theory behind quasi-static SCE and CCE solutions is presented in Hill (1950). The solution to the dynamic SCE approximation was developed by Hopkins (1960) and employed by Goodier (1965) to model the penetration of rigid and soft spheres into metal targets. Following the work in Goodier (1965), numerous authors (Forrestal et al., 1988; Chen et al., 2004; Chen and Li, 2002; Forrestal et al., 1987, 1990; Longcope and Forrestal, 1983; Masri and Durban, 2005, 2009; Warren and Forrestal, 1998) have developed analytical SCE and CCE models for both penetration and perforation problems. As shown by Forrestal and Warren (2008), the SCE approximation provides the best results for deep penetration problems. However, for perforation problems in which the target exhibits ductile hole growth, the CCE approximation provides the best results as discussed in Forrestal et al. (1990) and Forrestal and Warren (2009).

In this study, we first extend the CCE theory to include the Voce strain hardening rule. The Voce constitutive model allows the strain hardening rate to approach zero (i.e. the stress becomes constant) for large strains, as opposed to power-law constitutive models in which the stress continues to increase indefinitely with increasing strain. This is relevant for many materials (especially aluminum alloys) where the stress saturates at large strains (Holmen et al., 2015; Holmen et al., 2013). Next, we investigate how using Voce strain hardening, power-law strain hardening, and work equivalent (WEQ) elastic-perfectly plastic constitutive models in CCE approximations affects the ballistic limit velocities of rigid projectiles striking aluminum and steel target plates. Parameters for the constitutive models used in the CCE solutions are taken from equivalent stress versus logarithmic strain curves obtained from uniaxial tension tests of axisymmetric specimens of the materials under consideration. Finally, we evaluate the accuracy of the CCE approximations for the ballistic limit velocities from perforation experiments using 7.62mm APM2 bullets striking target plates made from a number of different aluminum and steel alloys. It will be shown that the CCE approximations are within $\pm 20\%$ of the experimental results for the 10 different configurations considered. This accuracy is comparable to the accuracy obtained using two-dimensional (2D) or three-dimensional (3D) nonlinear finite element (FE) simulations (Børvik et al., 2009; Flores-Johnson et al., 2011; Holmen et al., 2015; Holmen et al., 2013, 2017), but with much less effort to obtain the results.

Constitutive models

Three separate isotropic constitutive models are employed in this study to develop CCE approximations to predict ballistic limit and residual velocities of target configurations in which the primary mode of deformation is ductile hole growth. These are

$$\sigma = \begin{cases} E\varepsilon & \sigma \leq \sigma_0 \\ \sigma_0 + \sum_{i=1}^2 Q_i (1 - \exp(-C_i \varepsilon)) & \sigma > \sigma_0 \end{cases} \quad (1)$$

$$\sigma = \begin{cases} E\varepsilon & \sigma \leq \sigma_0 \\ \sigma_0 \left(\frac{E\varepsilon}{\sigma_0} \right)^n & \sigma > \sigma_0 \end{cases} \quad (2)$$

$$\sigma = \begin{cases} E\varepsilon & \sigma \leq \bar{\sigma}_0 \\ \bar{\sigma}_0 & \sigma > \bar{\sigma}_0 \end{cases} \quad (3)$$

where σ is the Cauchy (true) stress, ε is the logarithmic (true) strain, E is Young's modulus, and σ_0 is the quasi-static yield stress. Note that all constitutive relations presented above are formulated as functions of the total logarithmic strain ε , that is, the sum of the elastic and plastic strain.

Equation (1) gives the Voce strain hardening model, where (Q_i, C_i) are hardening parameters and $Q_1 + Q_2$ represents the saturated value of the strain hardening. Equation (2) gives the power-law hardening model, where n is the strain hardening exponent. Equation (3) gives the perfectly plastic WEQ model, where $\bar{\sigma}_0$ represents the yield stress to be determined so that the area under the equivalent stress-strain curve is equal for both the model and the experiment, namely

$$\bar{\sigma}_0 = \frac{1}{\varepsilon^*} \int_0^{\varepsilon^*} \sigma d\varepsilon \quad (4)$$

where ε^* is the true failure strain, ε_f , if we calibrate until failure, or the true necking strain, ε_{ln} , if we calibrate until necking in the specimen. Note also that the Cauchy stress is equal to the equivalent stress until necking takes place in a uniaxial tension test. The formation of a neck introduces a complex triaxial stress state in that region, and the value of the measured longitudinal stress required to cause plastic flow is increased. To account for the introduction of these triaxial stresses after necking, Bridgman corrections (Bridgman, 1964) are carried out before the constitutive equations are fit to the measured equivalent stress-strain curves. The details of this procedure are described in section "Target materials."

CCE solutions

In this section, we develop closed-form solutions for the dynamic expansion of a cylindrical cavity under plane strain conditions from zero initial radius in an infinite medium for elastic-plastic materials with the constitutive models defined by equations (1) through (3). With the CCE solutions, we require the plastic region to be incompressible and the elastic region to be compressible. A physically realistic solution is not possible if both the plastic and elastic regions are considered to be incompressible due to the fact that the radial stress becomes infinite at an infinite radial distance as discussed by Crozier and Hunter (1970). Furthermore, the stress state associated with the CCE problem is not a hydrostatic stress superposed on a uniaxial compressive stress, as with the SCE problem discussed by Hill (1950) and Luk et al. (1991). Therefore, a solution with both the plastic and elastic regions being compressible cannot be obtained for analytic CCE solution formulations. Note also that the global out-of-plane deformation of the plates is not accounted for in the model. This means that the model is only applicable in situations where ductile hole growth in the radial direction perpendicular to the projectile's axis of symmetry is the dominating deformation mode. In addition, only the rigid core of the APM2 projectile (Figures 1 and 3) is included in the derivation of the response equations.

The CCE approximation considers the target as a series of incremental layers perpendicular to the direction of perforation subjected to a radial CCE stress under plane strain conditions (Forrestal et al., 1981). Consequently, we require an axisymmetric cavity under plane strain conditions (where contractual strains are positive) to be expanded from a zero initial radius $a = 0$, as shown in Figure 2. This expansion produces plastic and elastic response regions. The plastic region is bounded by the radii $r = a$ and $r = b$, where r is the radial Eulerian coordinate, a is the cavity radius, $b = ct$ is the interface position between the plastic and elastic response regions, t is time, and c is the elastic-plastic interface velocity. Similarly, the elastic region is bounded by $r = b$ and $r = d$, where $d = c_d t$ and c_d is the elastic dilatational wave speed given by

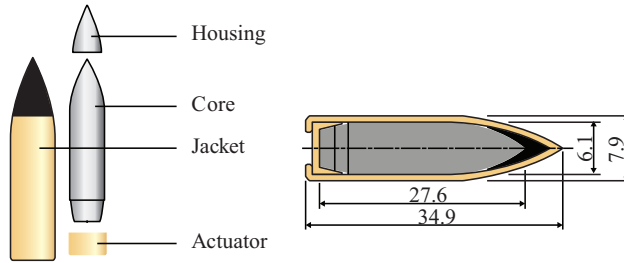


Figure 1. Schematic drawings and geometry of the 7.62 mm bullet (dimensions in mm).

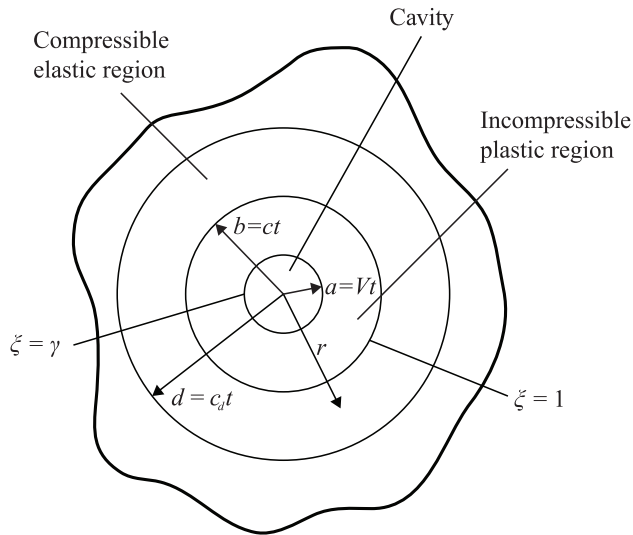


Figure 2. Cavity expansion approximation and different response regions.

$$c_d^2 = \frac{E(1-\nu)}{\rho(1+\nu)(1-2\nu)} \quad (5)$$

Here ν is Poisson's ratio, and ρ is the density which is assumed to be constant in the elastic region. For both regions, the equations for momentum and mass conservation in Eulerian coordinates with cylindrical symmetry are

$$\frac{\partial \sigma_r}{\partial r} + \frac{(\sigma_r - \sigma_\theta)}{r} = -\rho \left(\frac{\partial v}{\partial t} + v \frac{\partial v}{\partial r} \right) \quad (6a)$$

$$\rho_0 \frac{\partial}{\partial r} \left[(r-u)^2 \right] = 2\rho r \quad (6b)$$

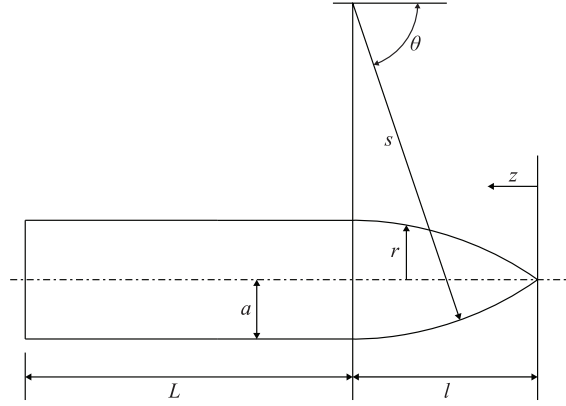


Figure 3. Ogival nose projectile with geometry.

where σ_r and σ_θ are the radial and circumferential components of the Cauchy stress that are positive in compression, ρ_0 and ρ are the material densities in the undeformed and deformed configurations, respectively, and v and u are the particle velocity and displacement in the radial direction (outward motion taken positive). These are related by the material time derivative as

$$\frac{\partial u}{\partial t} = v \left(1 - \frac{\partial u}{\partial r} \right) \quad (7)$$

Compressible elastic region

In the compressible elastic region, $b \leq r \leq d$, the response is the same for all three constitutive models given in equations (1) through (3). The response equations for the elastic region can be solved in various ways (e.g. Masri and Durban, 2009). However, we assume that the material is compressible and employ the similarity solution from Forrestal et al. (1990). The similarity solution requires the cavity to be expanded from zero initial radius, $a = 0$, at a constant velocity \dot{a} (i.e. $\ddot{a} \equiv 0$). It is assumed that displacements are small in the elastic region; thus, the strains can be assumed to be small, that is

$$\varepsilon_r = -\frac{\partial u}{\partial r} \quad (8a)$$

$$\varepsilon_\theta = -\frac{u}{r} \quad (8b)$$

Furthermore, we employ Hooke's law to obtain the stresses from the strains, that is

$$\sigma_r = \lambda(\varepsilon_r + \varepsilon_\theta) + 2\mu\varepsilon_r \quad (9a)$$

$$\sigma_\theta = \lambda(\varepsilon_r + \varepsilon_\theta) + 2\mu\varepsilon_\theta \quad (9b)$$

$$\sigma_z = \lambda(\varepsilon_r + \varepsilon_\theta) \quad (9c)$$

where λ and μ are the Lamé elastic constants given by

$$\lambda = \frac{\nu E}{(1+\nu)(1-2\nu)} \quad (10a)$$

$$\mu = \frac{E}{2(1+\nu)} \quad (10b)$$

Using equations (9a) to (10b) in equation (6a) and neglecting the convective acceleration term due to small deformations gives

$$-(\lambda + 2\mu) \frac{\partial^2 u}{\partial r^2} - (\lambda - 2\mu) \left[\frac{1}{r} \frac{\partial u}{\partial r} - \frac{u}{r^2} \right] = -\rho \frac{\partial^2 u}{\partial t^2} \quad (11)$$

Inserting equation (5) into equation (11) gives the second-order partial differential equation for conservation of linear momentum in the elastic region in terms of the particle displacement u as

$$\frac{\partial^2 u}{\partial r^2} + \frac{1}{r} \frac{\partial u}{\partial r} - \frac{u}{r^2} = \frac{1}{c_d^2} \frac{\partial^2 u}{\partial t^2} \quad (12)$$

Following Forrestal et al. (1990), we solve equation (12) using the dimensionless similarity transformation variable

$$\xi = \frac{r}{ct} \quad (13)$$

where c is the elastic–plastic interface velocity, and the dimensionless particle displacement \bar{u} , particle velocity U , and radial stress S are

$$\bar{u} = \frac{u}{ct} \quad (14a)$$

$$U = \frac{v}{c} = \bar{u} - \xi \frac{d\bar{u}}{d\xi} \quad (14b)$$

$$S = \frac{\sigma_r}{\sigma_0} = -\frac{E}{\sigma_0(1+\nu)(1-2\nu)} \left[\frac{d\bar{u}}{d\xi} + \nu \left(\frac{\bar{u}}{\xi} - \frac{d\bar{u}}{d\xi} \right) \right] \quad (14c)$$

Using equations (13) and (14a) in equation (12) gives the dimensionless homogeneous second-order ordinary differential equation

$$(1 - \omega^2 \xi^2) \frac{d^2 \bar{u}}{d\xi^2} + \frac{1}{\xi} \frac{d\bar{u}}{d\xi} - \frac{\bar{u}}{\xi^2} = 0 \quad (15)$$

where $\omega = (c/c_d)$. Next, we assume a first solution of the form $\bar{u} = \xi$ which satisfies equation (15). Using reduction of order, we assume a second solution of the form $\bar{u} = \xi\alpha$, where α is a function of ξ and equation (15) takes the form

$$\xi(1-\omega^2\xi^2)\frac{d^2\alpha}{d\xi^2} + (3-2\omega^2\xi^2)\frac{d\alpha}{d\xi} = 0 \quad (16)$$

We now set $\eta = d\alpha/d\xi$ which transforms equation (16) into the first-order homogeneous ordinary differential equation

$$\xi(1-\omega^2\xi^2)\frac{d\eta}{d\xi} + (3-2\omega^2\xi^2)\eta = 0 \quad (17)$$

which can be directly integrated giving the solution

$$\eta = \frac{C_1\sqrt{1-\omega^2\xi^2}}{\xi^3} \quad (18)$$

where C_1 is an integration constant. Using the already established relation $\eta = d\alpha/d\xi$, we do another integration $\int d\alpha = \int \eta d\xi$ which together with $\bar{u} = \xi\alpha$ gives

$$\bar{u} = C_1 \left[\frac{\xi\omega^2}{2} \ln \left(\frac{1+\sqrt{1-\omega^2\xi^2}}{\xi} \right) - \frac{\sqrt{1-\omega^2\xi^2}}{2\xi} \right] + C_2\xi \quad (19)$$

where C_2 is a second integration constant. At the elastic wave front $r = d$, the displacement $u = 0$; therefore, $\bar{u}(\xi = 1/\omega) = 0$ such that

$$\bar{u}(\xi = 1/\omega) = \frac{C_1\omega}{2} \ln(\omega) + \frac{1}{\omega}C_2 = 0 \quad (20)$$

$$C_2 = \frac{C_1\omega^2}{2} \ln \left(\frac{1}{\omega} \right) \quad (21)$$

Inserting equation (21) into equation (19) gives

$$\bar{u} = C_1 \left[\frac{\xi\omega^2}{2} \ln \left(\frac{1+\sqrt{1-\omega^2\xi^2}}{\omega\xi} \right) - \frac{\sqrt{1-\omega^2\xi^2}}{2\xi} \right] \quad (22)$$

At the elastic–plastic interface $r = b$, the von Mises yield criterion requires the principal stress difference to satisfy

$$\sigma_r(\xi = 1) - \sigma_\theta(\xi = 1) = \frac{2\sigma_0}{\sqrt{3}} = -2\mu C_1 \sqrt{1 - \omega^2} \quad (23)$$

Solving equation (23) for C_1 gives

$$C_1 = -\frac{2\sigma_0(1+\nu)}{\sqrt{3}E\sqrt{1-\omega^2}} \quad (24)$$

In the elastic region, $b \leq r \leq d$, the dimensionless particle displacement \bar{u} , particle velocity U , and radial stress S are then given by

$$\bar{u}(\xi) = \frac{\sigma_0(1+\nu)}{\sqrt{3}E\sqrt{1-\omega^2}} \left[\frac{\sqrt{1-\omega^2}\xi^2}{\xi} - \xi\omega^2 \ln \left(\frac{1+\sqrt{1-\omega^2}\xi^2}}{\omega\xi} \right) \right] \quad (25a)$$

$$U(\xi) = \frac{2\sigma_0(1+\nu)\sqrt{1-\omega^2}\xi^2}{\sqrt{3}E\xi\sqrt{1-\omega^2}} \quad (25b)$$

$$S(\xi) = \frac{\omega^2}{\sqrt{3}(1-2\nu)\sqrt{1-\omega^2}} \left[\ln \left(\frac{1+\sqrt{1-\omega^2}\xi^2}}{\omega\xi} \right) + \frac{(1-2\nu)\sqrt{1-\omega^2}\xi^2}}{\omega^2\xi^2} \right] \quad (25c)$$

On the elastic side of the elastic–plastic interface $r = b$ ($\xi = 1$), the dimensionless particle displacement \bar{u} , particle velocity U , and radial stress S are given by equation (25) as $\bar{u}(\xi = 1)$, $U(\xi = 1)$, and $S(\xi = 1)$, respectively.

Incompressible plastic region

In this section, we obtain the incompressible dynamic CCE solutions in the plastic region $a \leq r \leq b$ for the three constitutive models given by equations (1) through (3). We assume incompressibility, that is, $\rho = \rho_0$ in equation (6b) implying that Poisson's ratio ν is 0.5. Due to proportional (radial) loading conditions, total strain values can be employed; therefore, the total strains are equal to the sum of the total elastic and plastic components such that

$$\varepsilon_r = \varepsilon_r^e + \varepsilon_r^p \quad (26a)$$

$$\varepsilon_\theta = \varepsilon_\theta^e + \varepsilon_\theta^p \quad (26b)$$

The equivalent strain may also be used. For a uniaxial stress condition, the equivalent strain and von Mises stress are

$$\varepsilon_{\text{eq}} = |\varepsilon| \quad (27a)$$

$$\sigma_{\text{eq}} = |\sigma| \quad (27b)$$

where σ and ε are the Cauchy stress and logarithmic strain components in the axial direction of a uniaxial stress test. For an incompressible material with plane strain conditions $\sigma_z = (\sigma_r + \sigma_\theta) / 2$. For the CCE problem, the equivalent strain ε_{eq} and the equivalent stress σ_{eq} are related to the radial strain and Cauchy principal stress difference by

$$\varepsilon_{\text{eq}} = \frac{2}{\sqrt{3}} \varepsilon_r \quad (28a)$$

$$\sigma_{\text{eq}} = \frac{\sqrt{3}}{2} (\sigma_r - \sigma_\theta) \quad (28b)$$

In the plastic region, finite deformations are expected. Therefore, logarithmic radial and logarithmic circumferential strains are used, namely

$$\varepsilon_r = \ln \left(1 - \frac{\partial u}{\partial r} \right) \quad (29a)$$

$$\varepsilon_\theta = \ln \left(1 - \frac{u}{r} \right) \quad (29b)$$

We define an arbitrary elastic–plastic constitutive model $g(\varepsilon)$ to describe the principal stress difference in equation (6a) as a function of the radial strain, that is

$$\sigma_r - \sigma_\theta = \frac{2}{\sqrt{3}} g \left(\frac{2}{\sqrt{3}} \varepsilon_r \right) \quad (30)$$

We also define an additional dimensionless parameter

$$\gamma = \frac{V}{c} \quad (31)$$

which is the ratio of the cavity expansion velocity V to the elastic–plastic interface velocity c . Furthermore, we insert the similarity transformation variable ξ in equation (13), the dimensionless variables defined in equations (25a) to (25c), and the principal stress difference given in equation (30), into equations (6) for momentum and mass conservation, along with equation (7) for the material time derivative of the radial displacement. This transforms equations (6) and (7) into a set of ordinary differential equations given by

$$\frac{dS}{d\xi} + \frac{2}{\sqrt{3}\xi\sigma_0} g \left[\frac{2}{\sqrt{3}} \ln \left(1 - \frac{d\bar{u}}{d\xi} \right) \right] - \frac{\rho c^2}{\sigma_0} (\xi - U) \frac{dU}{d\xi} = 0 \quad (32a)$$

$$\frac{d}{d\xi} [(\xi - \bar{u})^2] = 2\xi \quad (32b)$$

$$U \left(1 - \frac{d\bar{u}}{d\xi} \right) = \bar{u} - \xi \frac{d\bar{u}}{d\xi} \quad (32c)$$

Replacing $g(2/\sqrt{3}(\varepsilon_r))$ with the constitutive models given by equations (1) through (3) in equation (32a) provides the ordinary homogeneous differential equations required to determine the radial stress at the cavity surface along with the elastic–plastic interface velocity.

At the cavity surface, $r = a$, the dimensionless displacement must satisfy

$$\bar{u}(\xi = \gamma) = \gamma \quad (33)$$

Additionally, at the elastic–plastic interface, Hugoniot interface conditions require that particle displacement, particle velocity, and traction normal to the interface to be continuous. Thus, on the elastic side of the elastic–plastic interface $\xi = 1$ ($r = b$), the dimensionless radial displacement, velocity, and radial stress are given by equation (25).

In the incompressible plastic region, the dimensionless conservation of linear momentum and mass, along with the material time derivative of the displacement, are given by equations (32a) to (32c). Integrating equation (32b) subject to the condition given by equation (33) gives

$$\bar{u} = \xi - (\xi^2 - \gamma^2)^{1/2} \quad (34)$$

Substituting equation (34) into equation (32c) reduces equation (32c) to

$$U = \frac{\bar{u} - \xi \frac{d\bar{u}}{d\xi}}{1 - \frac{d\bar{u}}{d\xi}} = \frac{\gamma^2}{\xi} \quad (35)$$

At the elastic–plastic interface $r = b$, the interface velocity, c , is obtained using equations (25b), (31), and (35), namely

$$\gamma = \frac{V}{c} = \sqrt{\frac{2(1+\nu)\sigma_0}{\sqrt{3}E}} \Rightarrow c = \sqrt{\frac{\sqrt{3}E}{2(1+\nu)\sigma_0}} V \quad (36)$$

The ratio, ω , of the elastic–plastic interface velocity c to the elastic dilatational wave speed c_d is then given as

$$\omega = \frac{c}{c_d} = V \sqrt{\frac{\sqrt{3}(1-2\nu)\rho}{2(1-\nu)\sigma_0}} \quad (37)$$

Voce strain hardening constitutive model

For the Voce strain hardening constitutive model, the principal stress difference is given by

$$\sigma_r - \sigma_\theta = \frac{2\sigma_0}{\sqrt{3}} \left[1 + \sum_{i=1}^2 \frac{Q_i}{\sigma_0} \left(1 - \exp\left(-\frac{2C_i}{\sqrt{3}} \varepsilon_r\right) \right) \right] \quad (38)$$

where $\sigma_r - \sigma_\theta \geq 2\sigma_0 / \sqrt{3}$, and ε_r is the logarithmic radial strain. Using equation (38) in equation (32a) gives

$$\frac{dS}{d\xi} + \frac{2}{\sqrt{3}\xi} \left\{ 1 + \sum_{i=1}^2 \frac{Q_i}{\sigma_0} \left[1 - \exp\left(-\frac{2C_i}{\sqrt{3}} \ln\left(1 - \frac{d\bar{u}}{d\xi}\right)\right) \right] \right\} - \frac{\rho c^2}{\sigma_0} (\xi - U) \frac{dU}{d\xi} = 0 \quad (39)$$

which simplifies to

$$\frac{dS}{d\xi} = \frac{\rho c^2}{\sigma_0} (\xi - U) \frac{dU}{d\xi} - \frac{2}{\sqrt{3}\xi} \left[1 + \sum_{i=1}^2 \frac{Q_i}{\sigma_0} \left[1 - \left(1 - \frac{d\bar{u}}{d\xi}\right)^{-\frac{2C_i}{\sqrt{3}}} \right] \right] \quad (40)$$

Integrating equation (40) throughout the plastic region as well as using equation (34) gives

$$S(\xi) = S(1) - \frac{2}{\sqrt{3}} \left\{ \ln(\xi) - \int_{\xi}^1 \frac{1}{\zeta} \sum_{i=1}^2 \frac{Q_i}{\sigma_0} \left[1 - \left(\frac{\zeta}{\sqrt{\zeta^2 - \gamma^2}} \right)^{-\frac{2C_i}{\sqrt{3}}} \right] d\zeta \right\} + \frac{\rho V^2}{2\sigma_0} \left[\gamma^2 - 2\ln(\xi) - \frac{\gamma^2}{\xi^2} \right] \quad (41)$$

where $S(1)$ is found from equation (25c). After rearranging the integral, we obtain

$$S(\xi) = \frac{1}{\sqrt{3}} (1 - \ln(\xi^2)) - \frac{2}{\sqrt{3}} \sum_{i=1}^2 \frac{Q_i}{\sigma_0} \left(\ln(\xi) + \frac{1}{2} \int_{\frac{1-\gamma^2}{1-\gamma/\xi^2}}^{1-\gamma^2} \frac{\zeta^{C_i/\sqrt{3}}}{1-\zeta} d\zeta \right) + \frac{\rho V^2}{2\sigma_0} \left[\gamma^2 - \ln(\xi^2) - \frac{\gamma^2}{\xi^2} + \frac{1}{(1-\nu)\sqrt{1-\omega^2}} \ln\left(\frac{1+\sqrt{1-\omega^2}}{\omega}\right) \right] \quad (42)$$

At the cavity surface $\xi = \gamma$, and equation (42) gives

$$S(\gamma) = \frac{1}{\sqrt{3}}(1 - \ln(\gamma^2)) - \frac{2}{\sqrt{3}} \sum_{i=1}^2 \frac{Q_i}{\sigma_0} \left(\ln(\gamma) + \frac{1}{2} \int_0^{1-\gamma^2} \frac{\zeta^{C_i/\sqrt{3}}}{1-\zeta} d\zeta \right) \quad (43)$$

$$+ \frac{\rho V^2}{2\sigma_0} \left[\gamma^2 - \ln(\gamma^2) - 1 + \frac{1}{(1-\nu)\sqrt{1-\omega^2}} \ln \left(\frac{1 + \sqrt{1-\omega^2}}{\omega} \right) \right]$$

Power-law strain hardening constitutive model

For the power-law strain hardening constitutive model, the principal stress difference is given by

$$\sigma_r - \sigma_\theta = \left[\frac{2}{\sqrt{3}} \right]^{1+n} E^n \sigma_0^{1-n} \varepsilon_r^n \quad (44)$$

where $\sigma_r - \sigma_\theta \geq 2\sigma_0 / \sqrt{3}$, and ε_r is the logarithmic radial strain. Using equation (44) in equation (32a) yields

$$\frac{dS}{d\xi} = - \left[\frac{2}{\sqrt{3}} \right]^{1+n} \left(\frac{E}{\sigma_0} \right)^n \frac{1}{\xi} \left[\ln \left(1 - \frac{d\bar{u}}{d\xi} \right) \right]^n + \frac{\rho c^2}{\sigma_0} (\xi - U) \frac{dU}{d\xi} \quad (45)$$

Integrating equation (45) throughout the plastic region as well as using equation (34) gives

$$S(\xi) = S(1) + \frac{2}{\sqrt{3}} \left[\frac{E}{\sqrt{3}\sigma_0} \right]^n \int_{\xi}^1 \frac{1}{\zeta} \left[\ln \left(\frac{\zeta^2}{\zeta^2 - \gamma^2} \right) \right]^n d\zeta + \frac{\rho V^2}{2\sigma_0} \left(\gamma^2 - \ln(\xi^2) - \frac{\gamma^2}{\xi^2} \right) \quad (46)$$

where $S(1)$ is taken from equation (25c). After rearranging the integral, we obtain

$$S(\xi) = \frac{1}{\sqrt{3}} \left[1 + \left[\frac{E}{\sqrt{3}\sigma_0} \right]^n \int_{1-(\gamma/\xi)^2}^{1-\gamma^2} \frac{(-\ln(\zeta))^n}{1-\zeta} d\zeta \right] \quad (47)$$

$$+ \frac{\rho V^2}{2\sigma_0} \left[\gamma^2 - \ln(\xi^2) - \frac{\gamma^2}{\xi^2} + \frac{1}{(1-\nu)\sqrt{1-\omega^2}} \ln \left(\frac{1 + \sqrt{1-\omega^2}}{\omega} \right) \right]$$

where, in general, the integral requires numerical integration using an open integration algorithm, see Press et al. (1989), due to the singularity at $\zeta = 0$. At the cavity surface $\xi = \gamma$, the dimensionless radial stress is

$$S(\gamma) = \frac{1}{\sqrt{3}} \left[1 + \left[\frac{E}{\sqrt{3}\sigma_0} \right]^n \int_0^{1-\gamma^2} \frac{(-\ln(\zeta))^n}{1-\zeta} d\zeta \right] + \frac{\rho V^2}{2\sigma_0} \left[\gamma^2 - \ln(\gamma^2) - 1 + \frac{1}{(1-\nu)\sqrt{1-\omega^2}} \ln \left(\frac{1+\sqrt{1-\omega^2}}{\omega} \right) \right] \quad (48)$$

Perfectly plastic WEQ constitutive model

For the elastic-perfectly plastic model, where $\bar{\sigma}_0$ is the yield stress found from equation (4), the principal stress difference is

$$\sigma_r - \sigma_\theta = \frac{2}{\sqrt{3}} \bar{\sigma}_0 \quad (49)$$

Using equation (49) in equation (32a) yields

$$\frac{dS}{d\xi} + \frac{2}{\sqrt{3}\xi} - \frac{\rho c^2}{\bar{\sigma}_0} (\xi - U) \frac{dU}{d\xi} = 0 \quad (50)$$

Integrating equation (50) throughout the plastic region as well as using equation (34) gives

$$S(\xi) = S(1) - \frac{1}{\sqrt{3}} \ln(\xi^2) + \frac{\rho V^2}{2\bar{\sigma}_0} \left(\gamma^2 - \ln(\xi^2) - \frac{\gamma^2}{\xi^2} \right) \quad (51)$$

where $S(1)$ is given in equation (25c), that is

$$S(\xi) = \frac{1}{\sqrt{3}} (1 - \ln(\xi^2)) + \frac{\rho V^2}{2\bar{\sigma}_0} \left[\gamma^2 - \ln(\xi^2) - \frac{\gamma^2}{\xi^2} + \frac{1}{(1-\nu)\sqrt{1-\omega^2}} \ln \left(\frac{1+\sqrt{1-\omega^2}}{\omega} \right) \right] \quad (52)$$

At the cavity surface $\xi = \gamma$, the dimensionless radial stress is

$$S(\gamma) = \frac{1}{\sqrt{3}} (1 - \ln(\gamma^2)) + \frac{\rho V^2}{2\bar{\sigma}_0} \left[\gamma^2 - \ln(\gamma^2) - 1 + \frac{1}{(1-\nu)\sqrt{1-\omega^2}} \ln \left(\frac{1+\sqrt{1-\omega^2}}{\omega} \right) \right] \quad (53)$$

The CCE approximation for perforation

To establish the CCE approximation for ductile hole growth perforation, we first obtain the radial Cauchy stress σ_r from the dimensionless radial stress S using the similarity transformation $S = \sigma_r / \sigma_0$, namely

$$\sigma_r = \sigma_0 S \quad (54)$$

From the three expressions obtained for the different constitutive models, we recognize that the radial stress consists of two terms: a static term and a term connected to the cavity expansion velocity V_r . Consequently, equation (54) may be recast as

$$\sigma_r = \sigma_s + B \rho V_r^2 \quad (55)$$

where σ_s is interpreted as the minimum stress required to open the cavity and B is given as

$$B = \frac{1}{2} \left[\frac{1}{(1-\nu)\sqrt{1-\omega^2}} \ln \left(\frac{1+\sqrt{1-\omega^2}}{\omega} \right) + \gamma^2 - 2 \ln(\gamma) - 1 \right] \quad (56)$$

Since γ and ω are both functions of the cavity expansion velocity, we further simplify equation (55) by approximating B in equation (56) by a consistent B_0 such that

$$\sigma_r = \sigma_s + B_0 \rho V_r^2 \quad (57)$$

where the B_0 parameter is obtained by curve fitting equation (55) to equation (57). Furthermore, we decompose the radial cavity expansion velocity, V_r , into its z -component (Figure 3), namely

$$V_r = V_z \frac{dr}{dz} \quad (58)$$

Neglecting friction, we find the incremental axial force acting on the projectile for a thin target layer with thickness dz as

$$dF_z = dF_r \frac{dr}{dz} \quad (59)$$

which gives the axial force

$$dF_r = \sigma_r dA \Rightarrow dF_z = 2\pi \sigma_r r(z) \frac{dr}{dz} dz \quad (60)$$

$$F_z = \int_0^l 2\pi r(z) \sigma_r \frac{dr}{dz} dz \quad (61)$$

Inserting equations (57) and (58) into equation (61) gives

$$F_z = 2\pi \left(\int_0^l \sigma_s r(z) \frac{dr}{dz} dz + \rho B_0 \int_0^l \left(V_z \frac{dr}{dz} \right)^2 r(z) \frac{dr}{dz} dz \right) \quad (62)$$

where

$$r(z) = (a - s) + \sqrt{s^2 - (l - z)^2} \quad (63a)$$

$$\frac{dr}{dz} = \frac{l - z}{\sqrt{s^2 - (l - z)^2}} \quad (63b)$$

Inserting equations (63a) and (63b) into equation (62) and carrying out the integration yields

$$F_z = \pi a^2 \left[\sigma_s + \rho B_0 N(\psi) V_z^2 \right] \quad (64)$$

where the nose shape coefficient is given as

$$N(\psi) = 8\psi^2 \ln \left(\frac{2\psi}{2\psi - 1} \right) - (4\psi + 1) \quad (65)$$

with ψ equal to the caliber radius head (CRH) and defined as

$$\psi = \frac{1}{4} \left[\left(\frac{l}{a} \right)^2 + 1 \right] \quad (66)$$

where l is equal to the projectile nose length, and a is the shank radius. To obtain the expression for the ballistic limit velocity, V_{bl} , and the residual velocity, V_{res} , we start from Newton's second law of motion, that is

$$m \frac{dV_z}{dt} + F_z = m V_z \frac{dV_z}{dz} + F_z = 0 \quad (67)$$

where m is the mass projectile given by (Forrestral and Warren, 2009)

$$m = \pi a^2 \rho_p (L + k_1 l) \quad (68)$$

where ρ_p is the projectile density, L is the projectile shank length, and k_1 is the ogive-nose shape parameter defined in terms of the ogive-nose CRH value, ψ , as

$$k_1 = \left(4\psi^2 - \frac{4\psi}{3} + \frac{1}{3} \right) - \frac{4\psi^2(2\psi - 1)}{\sqrt{4\psi - 1}} \arcsin \left(\frac{\sqrt{4\psi - 1}}{2\psi} \right) \quad (69)$$

Inserting equations (64) and (68) into equation (67), we obtain

$$\frac{V_z}{A + BV_z^2} dV_z = dz \quad (70a)$$

$$A = -\frac{\sigma_s}{\rho_p(L + k_1l)} \quad (70b)$$

$$B = -\frac{\rho B_0 N(\psi)}{\rho_p(L + k_1l)} \quad (70c)$$

To obtain the ballistic limit velocity, V_{bl} , the left-hand side of equation (70a) is integrated from V_{bl} to 0, while the right-hand side is integrated over the thickness, that is, from 0 to h . The ballistic limit velocity is thus found as

$$V_{bl} = \left[\frac{\sigma_s}{\rho B_0 N(\psi)} \left(\exp \left(\frac{2h}{(L + k_1l)} \frac{\rho}{\rho_p} B_0 N(\psi) \right) - 1 \right) \right]^{1/2} \quad (71)$$

Next, we obtain the residual velocity by integrating the left-hand side of equation (70a) from the striking velocity, V_s , to the residual velocity, V_{res} , namely

$$V_{res} = \sqrt{V_s^2 - V_{bl}^2} \exp \left[-\frac{h}{(L + k_1l)} \frac{\rho}{\rho_p} B_0 N(\psi) \right] \quad (72)$$

Since both the ballistic limit velocity and residual velocity equations are in terms of exponentials, they can be expanded in a power series, and if the argument is small, the series will converge quickly. Our argument is

$$\varphi = \frac{h}{(L + k_1l)} \frac{\rho}{\rho_p} B_0 N(\psi) \quad (73)$$

Table 1. Stress needed to open a cylindrical cavity from zero radius for the different constitutive models.

Model	σ_s (MPa)
Voce	$\frac{1}{\sqrt{3}} \left[\sigma_0 (1 - \ln(\gamma^2)) - \sum_{i=1}^2 Q_i \left(\ln(\gamma^2) + \int_0^{1-\gamma^2} \frac{x^{C_i/\sqrt{3}}}{1-x} dx \right) \right]$
Power	$\frac{\sigma_0}{\sqrt{3}} \left[1 + \left(\frac{E}{\sqrt{3}\sigma_0} \right)^n \int_0^{1-\gamma^2} \frac{(-\ln x)^n}{1-x} dx \right]$
WEQ	$\frac{\sigma_0}{\sqrt{3}} [1 - \ln(\gamma^2)]$

WEQ: work equivalent.

Algorithm 1. Procedure to find V_{bl} and V_{res} .

- 1: # Find B_0 in equation (57)
- 2: **while** $\omega^2 < 1$ (i.e. while B is real) **do**
- 3: Calculate σ_r from equation (55) for all cavity-
- 4: expansion velocities V_r giving real solutions.
- 5: **end while**
- 6: Do a curve fit of equation (57) to the calculated radial stresses σ_r as a function of cavity expansion velocity V_r to establish B_0 .
- 7: Calculate σ_s given in Table I for the respective constitutive model
- 8: Calculate V_{bl} using equation (74a)
- 9: Calculate V_{res} using equation (74b)

For large dense projectiles striking thin targets, the ballistic limit velocity and residual velocity can be approximated by

$$V_{bl} = \left(\frac{2\sigma_s}{\rho_p} \frac{h}{(L + k_1 l)} \right)^{1/2} \left[1 + \varphi + \frac{2}{3} \varphi^2 \right]^{1/2} \quad (74a)$$

$$V_{res} = \left(V_s^2 - V_{bl}^2 \right)^{1/2} \left[1 - \varphi + \frac{1}{2} \varphi^2 \right] \quad (74b)$$

Otherwise use equations (71) and (72) for more accurate results. The expressions for the quasi-static strength term σ_s for the different constitutive models given by equations (1) through (3) are presented in Table 1, while a simple algorithm describing the procedure used to obtain the ballistic limit velocity V_{bl} and the residual velocity V_{res} is given in Algorithm 1.

Materials and experimental data

Target materials

Of the ten configurations that we consider in this study, seven are aluminum alloys of different tempers and thicknesses, while the remaining three are steels. Specifically, we look at 20 mm plates of aluminum alloy AA6070 in four different tempers (Holmen et al., 2013), 10 mm and 30 mm thick plates of aluminum alloy AA6082-T6 (Holmen et al., 2015), 30 mm thick plates of the cast and homogenized aluminum alloy AA6060 (Westermann et al., 2014), 12 mm thick plates of the structural steel NVE 36 (Holmen et al., 2017), and 12 mm plates of the high-strength steels Weldox 500 E and Weldox 700 E (Børvik et al., 2009). Parameters for all the configurations are presented in Table 2.

Although the material tests were conducted in various studies reported in the literature, brief accounts of the testing and calibration procedures for the different materials are given below. Figures 4 to 6 show the equivalent stress versus longitudinal logarithmic strain curves (equivalent stress–strain curves) for all the configurations in this study. They were all obtained from uniaxial tension tests of cylindrical specimens with diameter of 6 mm and the initial strain rate in all the tests was $5.0 \times 10^{-4} \text{ s}^{-1}$. The force F was measured by a calibrated load cell in the hydraulic test machine and the current minimum cross-section area A of the gauge section was continuously measured all the way to fracture by a laser-scan micrometer placed on a moving frame. By assuming uniform stress and strain over the cross-section of the specimen as well as plastic incompressibility, the longitudinal Cauchy stress σ and longitudinal logarithmic strain ε can be found as

$$\sigma = \frac{F}{A}, \quad \varepsilon = \ln\left(\frac{A_0}{A}\right) \quad (75)$$

where A_0 is the initial area of the cross-section and A is the current area of the minimum cross-section. Note that the incompressibility assumption requires the elastic strain to be negligible compared to the plastic strain. To arrive at the equivalent stress σ_{eq} shown in Figures 4 to 6, the Cauchy stress was further corrected for triaxiality effects that appear after necking. This was done using Bridgman's analysis (Bridgman, 1964)

$$\sigma_{\text{eq}} = \frac{\sigma}{\left(1 + \frac{2R}{a}\right) \ln\left(1 + \frac{a}{2R}\right)} \quad (76)$$

where a is the specimen radius and R is the radius of the curvature of the neck. The geometry of the neck was estimated using an empirical relationship proposed by Le Roy et al. (1981)

$$\frac{a}{R} = 1.1(\varepsilon - \varepsilon_{\text{lu}}), \quad \varepsilon \geq \varepsilon_{\text{lu}} \quad (77)$$

where ε_{lu} is the strain at necking.

After obtaining the equivalent stress–strain curves, the parameters in the hardening rules were determined by minimizing the mean squared error between the experimental curves and the respective hardening rules in equations (1) to (3). The Voce hardening rule in equation (1) was fit to the

Table 2. Material constants for the various hardening rules for all the materials.

Material	To fracture										To neck			
	Voce					Power					WEQ			
	$\sigma_{0.2}$ (MPa)	σ_0 (MPa)	Q_1 (MPa)	C_1 (-)	Q_2 (MPa)	C_2 (-)	σ_0 (MPa)	n (-)	$\bar{\sigma}_0$ (MPa)	n (-)	$\bar{\sigma}_0$ (MPa)	Power	WEQ	ε_{lu} (-)
AA6070-O (Holmen et al., 2013)	51.2	41.9	85.09	46.34	90.97	2.99	54.91	0.2	180.7	0.24	141.7	43.9	141.7	0.21
AA6070-T4 (Holmen et al., 2013)	191.0	184.5	52.01	23.2	224.4	5.71	139.4	0.22	384.4	0.23	313.8	131.9	313.8	0.22
AA6070-T6 (Holmen et al., 2013)	381.7	342.0	48.3	184.3	74.97	7.16	372.3	0.05	420.1	0.04	353.2	378.8	353.2	0.06
AA6070-T7 (Holmen et al., 2013)	346.7	339.4	65.98	0.8	40.14	27.33	341.7	0.04	375.0	0.04	317.8	339.3	317.8	0.06
AA6082-T6-I0 (Holmen et al., 2015)	329.0	315.0	67.0	19.1	96.4	1.0	307.5	0.07	401.1	0.07	334.9	303.7	334.9	0.09
AA6082-T6-30 (Holmen et al., 2015)	279.9	265.3	144.4	0.38	67.8	26.54	270.5	0.06	341.4	0.08	288.7	258.4	288.7	0.08
AA6060 (Westermann et al., 2014)	71.7	68.1	68.6	26.4	114.5	3.9	52.2	0.24	207.3	0.27	163.5	42.1	163.5	0.23
NVE36 (Holmen et al., 2017)	387.4	298.1	280.3	17.7	576.8	0.7	236.3	0.19	769.2	0.22	530.9	201.1	530.9	0.20
Weldox 500 E (Børvik et al., 2009)	606.2	567.8	172.9	23.69	1356.0	0.22	470.2	0.12	936.3	0.1	665.5	521.6	665.5	0.10
Weldox 700 E (Børvik et al., 2009)	818.5	738.2	151.3	29.96	1980.0	0.13	672.8	0.09	1039.6	0.07	798.3	714.0	798.3	0.09

WEQ: work equivalent.

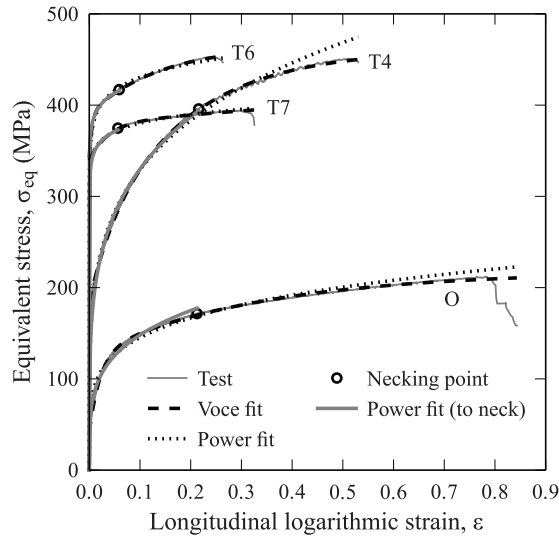


Figure 4. Bridgman corrected stress for AA6070 tempers.

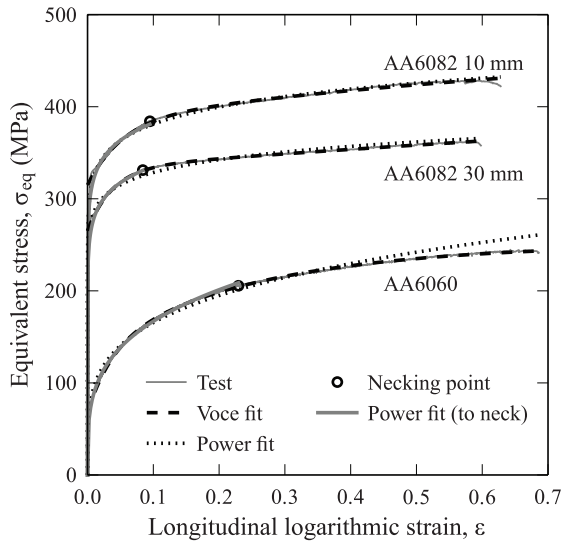


Figure 5. Bridgman corrected stress for AA6060 and AA6082-T6.

experimental data all the way to failure for all ten configurations. The power-law model (equation (2)) and the elastic-perfectly plastic WEQ model (equation (3)) were also calibrated all the way to failure for all configurations, but to assess the necessity of obtaining data after necking the fitting procedure was also stopped at the point of the neck which is marked with circles for each configuration in Figures 4 to 6. However, this was not done for the Voce strain hardening rule since the numerical fit to the experimentally determined equivalent stress–strain curve is very good. The need for a hardening rule which captures the saturation of the stress, such as the Voce hardening rule, is clearly seen from the equivalent stress–strain curves for the aluminum alloys in Figures 4 to 5.

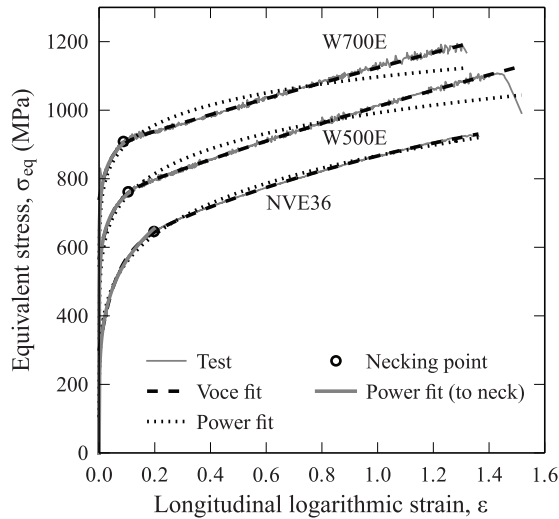


Figure 6. Bridgman corrected stress for NVE36, Weldox 500E, and Weldox 700E.

Ballistic testing

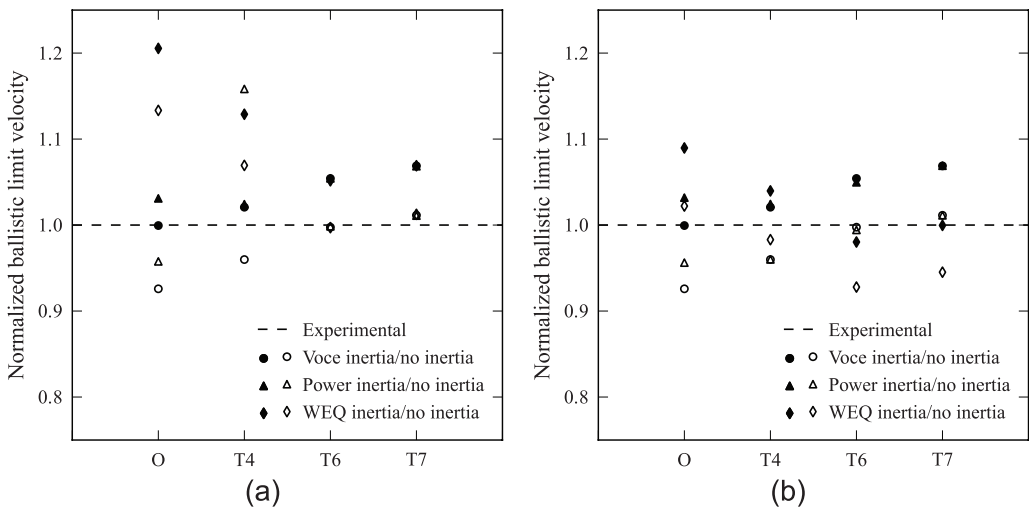
We used 7.62 mm armor piercing bullets in all ballistic tests in this study. However, only the 5 ± 0.25 g ogive-nose hardened steel core was used in the calculations. The effect of including the brass jacket was studied in Forrestal et al. (2010) and was found to reduce the ballistic limit velocity by between 1% and 11%. The hardened steel core has a CRH of 3.0, a Rockwell hardness R_C of 63, and a density of 7850 kg/m^3 . More information about the bullet and bullet materials can be found in Børvik et al. (2009).

All the ballistic tests were conducted using the same procedure. A smooth-bored Mauser rifle launched the projectiles at the target plates. The target plates were placed in a test fixture approximately 1 m from the muzzle of the gun. The impact velocity of the bullet could be predefined in advance by varying the amount of powder in the cartridge. During testing, the impact and residual velocities were measured with high-speed cameras; these images could also be used to assess the pitch and yaw of the bullet, which were found to be small and were considered to have negligible influence on the perforation behavior in any of the plates.

The ballistic programs referenced in this article were undertaken mainly to determine the ballistic limit velocity of the projectile–target configurations being considered. Determining the ballistic limit velocity with sufficient accuracy requires a number of tests. Bullets striking the plate at velocities lower than the ballistic limit velocity will not perforate the plate, while bullets striking the plates at velocities higher than the ballistic limit velocity will perforate the target and retain some residual velocity. Detailed descriptions of the ballistic studies relevant to this study can be found in the literature: Holmen et al. (2013) describe the procedure for 20 mm thick AA6070 aluminum plates with tempers O, T4, T6, and T7; Holmen et al., (2015) present the results for AA6082-T6 plates with thicknesses of 10 and 30 mm; Frodal and Valle (2015) report the ballistic study on 30 mm thick specimens of AA6060; 12 mm NVE 36 steel plates were tested in Holmen et al. (2017), while Weldox 500 E and Weldox 700 E were tested in Børvik et al. (2009). A summary of the experimental ballistic results is given in Table 3.

Table 3. Ballistic limits of all the configurations considered in this study.

Material	V_{bl} (m/s)	Plate thickness (mm)
AA6070-O (Holmen et al., 2013)	348	20
AA6070-T4 (Holmen et al., 2013)	506	20
AA6070-T6 (Holmen et al., 2013)	563	20
AA6070-T7 (Holmen et al., 2013)	529	20
AA6082-T6 (Holmen et al., 2015)	347	10
AA6082-T6 (Holmen et al., 2015)	581	30
AA6060 (Frodal and Valle, 2015)	518	30
NVE36 (Holmen et al., 2017)	579	12
Weldox 500 E (Børvik et al., 2009)	624	12 (2×6)
Weldox 700 E (Børvik et al., 2009)	675	12 (2×6)

**Figure 7.** Results from CCET analyses on the AA6070 aluminum alloy: (a) shows results for calibration up to fracture and (b) shows results for calibration up to neck.

Results and discussion

The results from the CCE analyses can be seen in Figures 7 to 9. Subfigure (a) shows the results obtained using the three different models when the entire equivalent stress–strain curve was fitted, and subfigure (b) shows the results obtained when fitting the models up to necking only (except for the Voce strain hardening rule). We conducted analyses both with and without inertia effects. All results are normalized with respect to their corresponding experimentally determined ballistic limit velocity and presented as functions of the target configuration. We find that the results are generally good for all three constitutive models, since they are in good agreement with the experimental values. Figure 10 directly compares the numerical results to the experimental data. The largest deviations between the numerical and experimental ballistic limit velocities are about $\pm 20\%$. However, many of the results are non-conservative, and this is especially pronounced for the simulations where inertia effects were accounted for. The analyses where inertia was omitted lie below

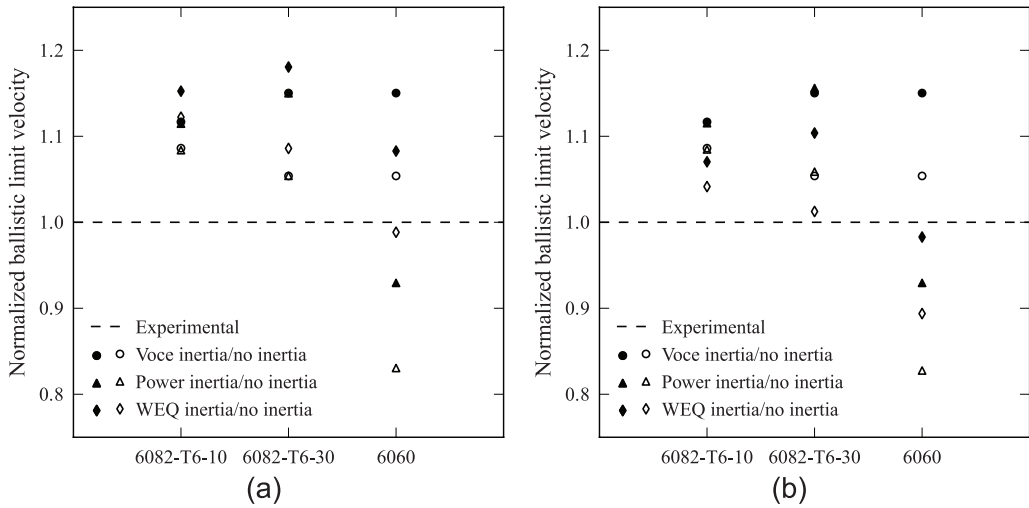


Figure 8. Results from CCET analyses on the AA6082 and AlMgSi aluminum alloys: (a) shows results for calibration up to fracture and (b) shows results for calibration up to neck.

the results including inertia. This implies that neglecting target inertia gives a conservative result. Warren (2016) recently reviewed the effects of inertia in the case of deep penetration using SCE approximations and concluded that the effect of inertia is limited at low impact velocities ($V_s < 500$ m/s for the projectile–target configurations considered). Another source contributing to non-conservative results is the omission of the brass jacket. As mentioned earlier, an experimental study by Forrestal et al. (2010) showed that including the brass jacket will generally reduce the predicted ballistic limit velocity by less than 10%.

Figure 7 presents the results for the four different tempers of aluminum alloy AA6070. By comparing Figure 7a to Figure 7b, we observe that the results are generally less scattered when the calibration of the constitutive model is done up to diffuse necking. This suggests that it is probably more important to describe the stress–strain behavior up to instability than up to fracture for this type of analytical model. The same trend is observed in Figure 8, where results for AA6082-T6 and AA6060 aluminum alloys are shown, and the results for the three different steels are illustrated in Figure 9. However, for two configurations, the scatter increases when calibrating the models up to necking, namely AA6070 in tempers T6 and T7. The reason might be that these alloys fragmented during the perforation process. Note that CCE analyses assume ductile hole growth and cannot describe fragmentation; thus, the correct physical mechanism is not captured in the analysis for AA6070-T6 and T7. The causes and effects of target fragmentation are discussed in Holmen et al. (2013, 2016).

The general trend from our CCE analyses in this study is that the results are non-conservative, that is, that the predicted ballistic limit velocity is too high. Since the constitutive models have been calibrated based on quasi-static and isothermal equivalent stress–strain curves obtained at room temperature, the effects of thermal softening and strain rate hardening have not been accounted for. Strain rate effects can be accounted for with the CCE approximations following the approach by Warren (1999). Detailed analysis of the temperature dependence of the ballistic limit velocity is given by Masri (2014). Børvik et al. (2009) showed that by calibrating a power strain hardening rule to equivalent stress–strain curves obtained at elevated temperatures would reduce the ballistic

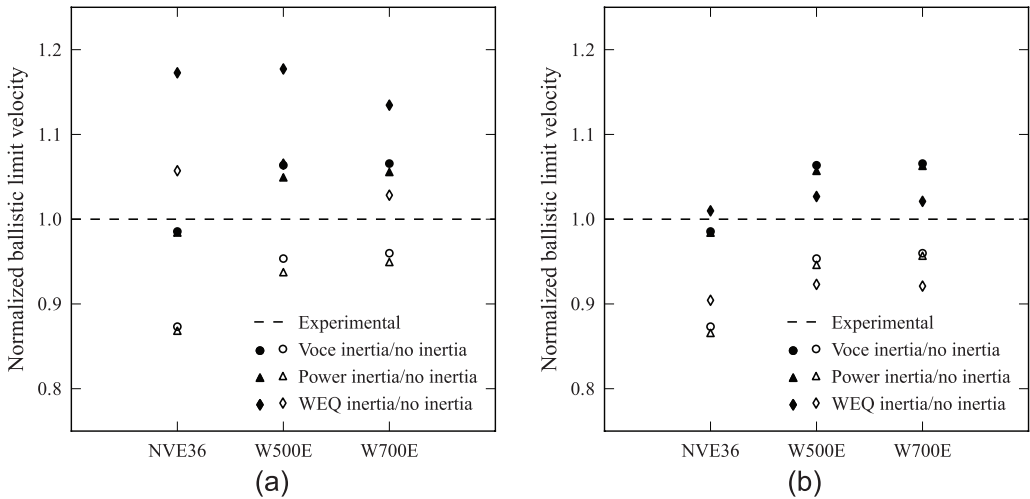


Figure 9. Results from CCET analyses on the NVE36, Weldox 500E, and Weldox 700E steel alloys: (a) shows results for calibration up to fracture and (b) shows results for calibration up to neck.

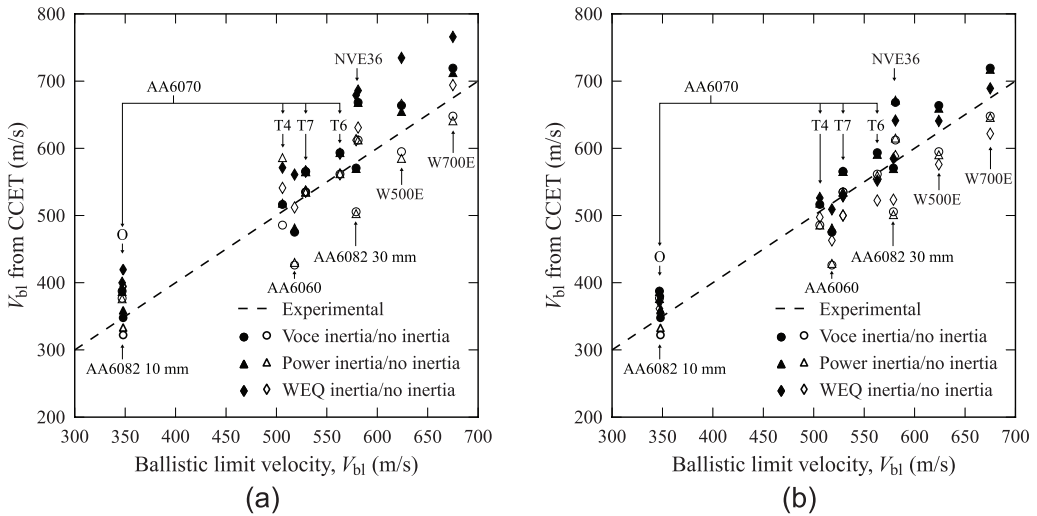


Figure 10. Results from CCET analyses for all investigated materials: (a) shows results for calibration up to fracture and (b) shows results for calibration up to neck.

limit velocity to a more conservative value. It was also found that by neglecting thermal softening and strain rate hardening in FE simulations, these simulations would give nearly identical results as CCE analyses. Their results suggest that under similar circumstances with identical assumptions, the CCE approximation and FE simulations will give similar results (Børvik et al., 2009). The analytical CCE approximation provides ductile hole growth perforation results significantly faster than numerical simulations; however, it does lack the problem statement flexibility of FE simulations (see e.g. Holmen et al., 2017).

Concluding remarks

In this study, we have presented the complete derivation of the CCE approximation with three different constitutive models. Data from material and ballistic tests for ten different materials were revisited before CCE analyses of all the configurations with various calibrations for the three constitutive relations were conducted.

The overall ballistic limit velocities obtained by the CCE analyses are in good agreement with the experimentally obtained ballistic limit velocities. No result differs by more than 20% from its corresponding experimentally determined value. Calibrating the material constitutive model up to necking reduces the scatter between the constitutive models. This is the case for all materials except the T6 and T7 tempers of the AA6070 alloy, and the AA6060 alloy. For the remaining materials, the CCE approximation gives results within $\pm 10\%$ of the experimental values when the constitutive models are fitted up to necking in the stress–strain curve. This accuracy is comparable to the results obtained from more advanced nonlinear 2D or 3D FE simulations (Børvik et al., 2009; Flores-Johnson et al., 2011; Holmen and Børvik, 2015; Holmen et al., 2013, 2017).

Our analysis suggests that the choice of constitutive model plays a minor role in the end result of a CCE analysis if we only look at material data up to diffuse necking. An alternative to calibrating the material up to necking is to use the so-called cavitation stress (Masri and Durban, 2009). If we calibrate up to fracture, the Voce strain hardening rule gives better results. However, the complexity of the derivation of the CCE approximation, and the equation for the required stress to open a cavity σ_s , increases significantly when using the Voce strain hardening rule compared to the simpler perfectly plastic WEQ model. This means that simple material tests can be used for the calibration of material constants to be used in CCE analyses which is beneficial from a practical point of view since we can obtain sufficiently accurate V_{bl} using a minimum of material parameters.

Acknowledgements

The authors thank Dr. Michael J. Forrestal for being an important discussion partner in the work regarding the cavity expansion theory.

Declaration of conflicting interests

The author(s) declared no potential conflicts of interest with respect to the research, authorship, and/or publication of this article.

Funding

The author(s) disclosed receipt of the following financial support for the research, authorship, and/or publication of this article: Financial support from this work comes from the Research Council of Norway (project no. 237885) through the Centre for Advanced Structural Analysis (SFI CASA) at the Norwegian University of Science and Technology and from Thomas L. Warren, Ph.D. Inc. Their contributions are greatly appreciated.

ORCID iD

Joakim Johnsen  <http://orcid.org/0000-0001-6110-9841>

References

Bishop RF, Hill R and Mott NF (1945) The theory of indentation and hardness tests. *Proceedings of the Physical Society* 57: 147–159.

- Børvik T, Dey S and Clausen AH (2009) Perforation resistance of five different high-strength steel plates subjected to small-arms projectiles. *International Journal of Impact Engineering* 36: 948–964.
- Børvik T, Forrestal MJ, Hopperstad OS, et al. (2009) Perforation of AA5083-H116 aluminium plates with conical-nose steel projectiles – Calculations. *International Journal of Impact Engineering* 36: 426–437.
- Bridgman PW (1964) *Studies in Large Plastic Flow and Fracture: With Special Emphasis on the Effects of Hydrostatic Pressure* (Metallurgy and metallurgical engineering series). Cambridge, MA: Harvard University Press.
- Chen XW and Li QM (2002) Deep penetration of a non-deformable projectile with different geometrical characteristics. *International Journal of Impact Engineering* 27: 619–637.
- Chen XW, Fan SC and Li QM (2004) Oblique and normal perforation of concrete targets by a rigid projectile. *International Journal of Impact Engineering* 30: 617–637.
- Crozier RJM and Hunter SC (1970) Similarity solution for the rapid uniform expansion of a cylindrical cavity in a compressible elastic-plastic solid. *The Quarterly Journal of Mechanics & Applied Mathematics* 23: 349–363.
- Flores-Johnson EA, Saleh M and Edwards L (2011) Ballistic performance of multi-layered metallic plates impacted by a 7.62-mm APM2 projectile. *International Journal of Impact Engineering* 38: 1022–1032.
- Forrestal MJ and Warren TL (2008) Penetration equations for ogive-nose rods into aluminum targets. *International Journal of Impact Engineering* 35: 727–730.
- Forrestal MJ and Warren TL (2009) Perforation equations for conical and ogival nose rigid projectiles into aluminum plate targets. *International Journal of Impact Engineering* 36: 220–225.
- Forrestal MJ, Børvik T and Warren TL (2010) Perforation of 7075-T651 aluminum armor plates with ogive-nose rods and 7.62 mm APM2 bullets. *Experimental Mechanics* 50: 1245–1251.
- Forrestal MJ, Luk VK and Brar NS (1990) Perforation of aluminum armor plates with conical-nose projectiles. *Mechanics of Materials* 10: 97–105.
- Forrestal MJ, Norwood FR and Longcope DB (1981) Penetration into targets described by locked hydrostats and shear strength. *International Journal of Solids and Structures* 17(9) 915–924.
- Forrestal MJ, Okajima K and Luk VK (1988) Penetration of 6061-T651 aluminum targets with rigid long rods. *Journal of Applied Mechanics* 55: 755–760.
- Forrestal MJ, Rosenberg Z, Luk VK, et al. (1987) Perforation of aluminum plates with conical-nosed rods. *Journal of Applied Mechanics* 54: 230–232.
- Frodal BH and Valle H (2015) *A multi-scale approach for modelling of fracture in aluminium alloys under impact loading*. Master's Thesis, Norwegian University of Science and Technology, Trondheim.
- Goodier JM (1965) On the mechanics of indentation and cratering in solid targets of strain-hardening metal by impact of hard and soft spheres. AIAA: Proceedings of the 7th Symposium on Hypervelocity Impact III: 215–259.
- Hill (1950) *The Mathematical Theory of Plasticity*. Oxford: Oxford University Press.
- Holmen JK, Børvik T, Myhr OR, et al., (2015) Perforation of welded aluminum components: microstructure-based modeling and experimental validation. *International Journal of Impact Engineering* 84: 96–107.
- Holmen JK, Børvik T and Hopperstad OS (2017) Experiments and simulations of empty and sand-filled aluminum alloy panels subjected to ballistic impact. *Engineering Structures* 130: 216–228.
- Holmen JK, Johnsen J, Hopperstad OS, et al. (2016) Influence of fragmentation on the capacity of aluminum alloy plates subjected to ballistic impact. *European Journal of Mechanics—A/Solids* 55: 221–233.
- Holmen JK, Johnsen J, Jupp S, et al. (2013) Effects of heat treatment on the ballistic properties of AA6070 aluminium alloy. *International Journal of Impact Engineering* 57: 119–133.
- Holmen JK, Solberg JK, Hopperstad OS, et al. (2017) Ballistic impact of layered and case-hardened steel plates. *International Journal of Impact Engineering* 110: 4–14.
- Hopkins HG (1960) Chapter 3: Dynamic expansion of spherical cavities in metals. In: Sneddon IN and Hill R (eds) *Progress in Solid Mechanics*, vol. 1. New York: North-Holland Publishing Company, pp. 85–164.
- Le Roy G, Embury JD and Ashby MF (1981) A model of ductile fracture based on the nucleation and growth of voids. *Acta Metallurgica* 29: 1509–1522.
- Longcope DB and Forrestal MJ (1983) Penetration of targets described by a Mohr-Coulomb failure criterion with a tension cutoff. *Journal of Applied Mechanics* 50: 327–333.

- Luk VK, Forrestal MJ and Amos DE (1991) Dynamic spherical cavity expansion of strain-hardening metals. *Journal of Applied Mechanics* 58: 1–6.
- Masri R (2014) The effect of adiabatic thermal softening on specific cavitation energy and ductile plate perforation. *International Journal of Impact Engineering* 68: 15–27.
- Masri R and Durban D (2005) Dynamic spherical cavity expansion in an elastoplastic compressible Mises solid. *Journal of Applied Mechanics* 72: 887–898.
- Masri R and Durban D (2009) Deep penetration analysis with dynamic cylindrical cavitation fields. *International Journal of Impact Engineering* 36: 830–841.
- Press WH, Flannery BP, Teukolsky SA, et al. (1989) *Numerical Recipes: The Art of Scientific Computing*. Cambridge: Cambridge University Press.
- Rosenberg Z and Dekel E (2012) *Terminal Ballistics*. Berlin: Springer.
- Warren TL (1999) The effect of strain rate on the dynamic expansion of cylindrical cavities. *Journal of Applied Mechanics* 66: 818–821.
- Warren TL (2016) The effect of target inertia on the penetration of aluminum targets by rigid ogive-nosed long rods. *International Journal of Impact Engineering* 91: 6–13.
- Warren TL and Forrestal MJ (1998) Effects of strain hardening and strain-rate sensitivity on the penetration of aluminum targets with spherical-nosed rods. *International Journal of Solids and Structures* 35: 3737–3753.
- Westermann I, Pedersen KO, Furu T, et al. (2014) Effects of particles and solutes on strength, work-hardening and ductile fracture of aluminium alloys. *Mechanics of Materials* 79: 58–72.